

Distribution Agreement

In presenting this thesis as a partial fulfillment of the requirements for a degree from Emory University, I hereby grant to Emory University and its agents the non-exclusive license to archive, make accessible, and display my thesis in whole or in part in all forms of media, now or hereafter now, including display on the World Wide Web. I understand that I may select some access restrictions as part of the online submission of this thesis. I retain all ownership rights to the copyright of the thesis. I also retain the right to use in future works (such as articles or books) all or part of this thesis.

Edrick Wang

April 9th, 2025

Higher-order Van Hove singularities in kagome topological bands

by

Edrick Wang

Luiz H. Santos
Adviser

Physics Department

Luiz H. Santos
Adviser

Ajit Srivastava
Committee Member

Wladimir Benalcazar
Committee Member

2025

Higher-order Van Hove singularities in kagome topological bands

By

Edrick Wang

Luiz H. Santos
Adviser

An abstract of
a thesis submitted to the Faculty of Emory College of Arts and Sciences
of Emory University in partial fulfillment
of the requirements of the degree of
Bachelor of Science with Honors

Physics Department

2025

Abstract

Higher-order Van Hove singularities in kagome topological bands

By Edrick Wang

Motivated by the growing interest in band structures featuring higher-order Van Hove singularities (HOVHS), we investigate a spinless fermion kagome system characterized by nearest-neighbor (NN) and next-nearest-neighbor (NNN) hopping amplitudes. While NN hopping preserves time-reversal symmetry, NNN hopping, akin to chiral hopping on the Haldane lattice, breaks time-reversal symmetry and leads to the formation of topological bands with Chern numbers ranging from $C = \pm 1$ to ± 4 . We perform analytical and numerical analysis of the energy bands near the high-symmetry points Γ , $\pm\mathbf{K}$, and \mathbf{M}_i ($i = 1, 2$, and 3), which uncover a rich and complex landscape of HOVHS, controlled by the magnitude and phase of the NNN hopping. We observe power-law divergences in the density of states (DOS), $\rho(\epsilon) \sim |\epsilon|^{-\nu}$, with exponents $\nu = 1/2, 1/3, 1/4$, which can significantly affect the anomalous Hall response at low temperatures when the Fermi level crosses the HOVHS. Additionally, the NNN hopping induces the formation of higher Chern number bands $C = \pm 2, \pm 4$ in the middle of the spectrum obeying a sublattice interference whereupon electronic states are maximally localized in each of the sublattices when the momentum approaches the three high-symmetry points \mathbf{M}_i ($i = 1, 2$, and 3) on the Brillouin zone boundary. This classification of HOVHS in kagome systems provides a platform to explore unconventional electronic orders induced by electronic correlations.

Higher-order Van Hove singularities in kagome topological bands

By

Edrick Wang

Luiz H. Santos
Adviser

A thesis submitted to the Faculty of Emory College of Arts and Sciences
of Emory University in partial fulfillment
of the requirements of the degree of
Bachelor of Science with Honors

Physics Department

2025

Acknowledgements

First, I would like to express my immense gratitude towards my advisor Luiz H. Santos, who, throughout my undergraduate years, has given me countless exceptional lectures and taught me to always be curious about nature. I am very glad to have someone who is also interested in language to be my physics research advisor. Most importantly, he has shown me what it means to be an outstanding theoretical physicist. I also wish to thank my graduate student group members, Lakshmi Pullasserri and Tianhong Lu, who have always been patient and encouraging with my learning journey in the condensed matter field at Emory. For the Band Topology section, I would like to thank Lakshmi Pullasserri again for her indispensable contribution on the anomalous Hall response calculations.

I thank Ajit Srivastava for serving on this committee and teaching me the fundamentals of the solid state physics, and Wladimir Benalcazar for also being on the committee and guiding me through the intriguing world of topological condensed matter.

I am also grateful to the faculty I've met on my physics journey at Emory. Specifically, I would like to thank Merida Batiste, who has given me tremendous support and mentorship in my computational astrophysics research from 2022 to 2024. The amount of invaluable computational skills I acquired enabled me to come this far as a scientist. I would also like to express thanks to Erin Bonning, who has been a professor to me since 2022. From cosmology to general relativity, the knowledge which she has passed down to me and countless others are to be never forgotten.

I would also like to thank all the physics friends I have made at Emory. Specifically, I would like to thank Zach Hadjri and Kristen Gram for our friendships over the past three years. They have been an extremely positive influence in my undergraduate physics career, especially my decision to continue condensed matter, and I will never forget the late night study sessions and physics talks we have at our apartments.

Finally, I would like to express my gratitude to my family, as they have given me unconditional support throughout the years with my decision to study physics and linguistics.

Contents

1	Introduction	1
2	Background	5
2.1	Kagome Systems	5
2.2	Van Hove Singularities	6
2.3	Berry Curvature	7
3	Model	9
4	Analysis	11
4.1	Higher-order Van Hove Singularities	11
4.1.1	Critical Points at $\pm\mathbf{K}$	13
4.1.2	Critical Points at Γ	14
4.1.3	Critical Points at \mathbf{M}_i	15
4.1.4	HOVHS Phase Diagrams	16
4.2	Band Topology	19
4.3	Sublattice Interference	22
5	Conclusion	24
A	Analytical Expressions of the HOVHS Lines	26
	Bibliography	29

List of Figures

1.1	An illustration of (a) the honeycomb lattice, the underlying lattice structure of graphene, and (b) the kagome lattice, which is the system of interest in this thesis.	1
2.1	A conventional saddle point on a 2-dimensional manifold. The Taylor expansion around the saddle point reads $z \propto x^2 - y^2$	6
2.2	Example of Berry curvature using the Fukui method. The Chern number resulting from this curvature is 1.	8
3.1	Kagome lattice with the sites A, B, and C marked in orange, blue, and green respectively. The vectors connecting site B with its nearest neighbors A and C are denoted as \mathbf{a}_2 and \mathbf{a}_1 respectively. The real NN hopping amplitude, t_1 , is represented by solid black lines. The black dashed arrows show the orientation of the NNN hoppings with strength $t_2 e^{i\phi}$. This NNN hopping breaks time-reversal symmetry while preserving \mathcal{C}_3 rotation and inversion symmetry about the center of the hexagon.	10

4.1	Band structure at (a) $(t_2, \phi) = (0, 0)$ and (b) $(t_2, \phi) = (0.76, 0.9\pi)$, with the first BZ shown in (a). The corresponding DOS is displayed on the right. The red dashed lines in (a) and (b) denote the energy at which the M points of the second band support a conventional VHS and a HOVHS respectively, as indicated by the divergences in the corresponding DOS. Notice that the energy corresponding to the M points on band 2 is always zero.	12
4.2	Contour plots of the energy dispersion corresponding to band 2, near the high-symmetry point $\pm K$. The white lines denote the boundaries of the first BZ and the black lines correspond to the Fermi surface contour at the corresponding energy of the HOVHS. The dispersion here exhibits a monkey-saddle dispersion.	13
4.3	Contour plots of the energy dispersion corresponding to band 2, near the high-symmetry point Γ where the Hessian vanishes, thereby supporting HOVHS. At the Γ point (a), which is an extremum, the second-order curvature of the dispersion vanishes along both k_x and k_y directions. (b) The energy dispersion considered in (a), around the Γ point, plotted along k_x with k_y held constant at zero, in order to highlight the flatness of the band around the Γ point.	14
4.4	Contour plots of the energy dispersion corresponding to band 2, near the high-symmetry point M_i where the Hessian vanishes, thereby supporting HOVHS. Around the M_3 point, the dispersion becomes locally flat only along the k_x direction.	16

4.5 (a)-(c) Parameter space plots showing the set of (t_2, ϕ) values for which the high-symmetry points Γ (orange), $\pm K$ (blue) and M (green) corresponding to the bands 1-3 (from left to right) support HOVHSs. The dashed lines correspond to the high-symmetry points which can be classified as higher-order saddles whereas the solid lines correspond to extrema with vanishing Hessian. (d) Parameter space plot zoomed in around the intersections of the lines highlighted with the black dashed lines in (a), clarifying the different intersections of boundary lines. The parameter pair of interest is labeled with \star , with values $(t_2 = 0.45, \phi = 0.76\pi)$. (e) The 3D plot of the band structure at parameters labeled with \star in (d), supporting HOVHSs at both M and Γ points. The energy value corresponding to the HOVHS at the M and Γ points are $-2.74 t_1$ and $-2.67 t_1$ respectively. (f) Band diagram of the same bands to showcase the exceptional flatness of band 1, with an approximate bandwidth of $0.08 t_1$. The first BZ is shown in the diagram as well. 17

- 4.6 Phase diagrams for band 1 (left), band 2 (middle), and band 3 (right), showing the corresponding Chern numbers in the t_2 - ϕ parameter space. Since TRS is respected at $\phi = 0, \pi$, the Chern number for all three bands at $\phi = 0, \pi$ are 0. White regions in the phase diagrams indicate non-positive indirect energy gaps where the Chern number is not well-defined. (In this case, there is no situation where the Fermi energy lies in between the bands, and the bands are characterized by a possible non-quantized anomalous Hall response.) Only $[0, \pi]$ is shown on the ϕ axis, since for any Chern number C at (t_2, ϕ) , as ϕ goes to $-\phi$, the Chern number flips sign. As seen in certain regions of the parameter space, band 2 can support Chern number as high as ± 4 20
- 4.7 (a-c) Intrinsic anomalous Hall conductivity $\sigma_{xy}^{\text{int}}(\mu; 0)$ and (d-f) the corresponding differential anomalous Hall conductivity $\frac{d\sigma_{xy}^{\text{int}}(\mu; 0)}{d\mu}$ at zero temperature, plotted as a function of the Fermi energy μ in units of t_1 for the Chern bands supporting HOVHS at $(t_2, \phi) = (0.39, \pi/2)$ for band 1 (left), $(t_2, \phi) = (0.26, \pi/2)$ for band 2 (middle) and $(t_2, \phi) = (0.80, -0.9\pi)$ for band 3 (right). The high-symmetry point where the HOVHS is located is mentioned in each plot. The differential anomalous Hall response, like the corresponding DOS, exhibits a power-law divergence around μ^* (marked by the blue dashed line) with exponents $1/3, 1/4$ and $1/2$ for K, M and Γ point respectively. 21

- 4.8 Contour plot of the sublattice weights for the second band corresponding to the sites A (left), B (middle), and C (right) of the kagome lattice at $(t_2, \phi) = (0.258, \pi/2)$, demonstrating that each M_i point on band 2 corresponds to one of the three sites of the kagome lattice. In this example, the band carries a Chern number of +2 while supporting HOVHS at the M points. Here, the black lines denote the first Brillouin zone boundaries. 23

Chapter 1

Introduction

Since the birth of solid state physics, the primary objects to study are 3-dimensional (3D) materials, which exist naturally in nature. Recently, experimental methods such as exfoliation methods are utilized, such that individual layers of atoms can be separated with ease. Graphene, which is one layer of graphite, is the first and a common example of 2D materials (Fig. 1.1 (a)) [1]. Although 2D materials still consist of atoms which are 3-dimensional, they can be approximately treated as 2-dimensional. The length scale at which electrons can travel in the z-direction is so small compared to the other 2 degrees of freedom (x and y), that the electrons are essentially constrained to only the xy-plane, thus a 2D lattice system.

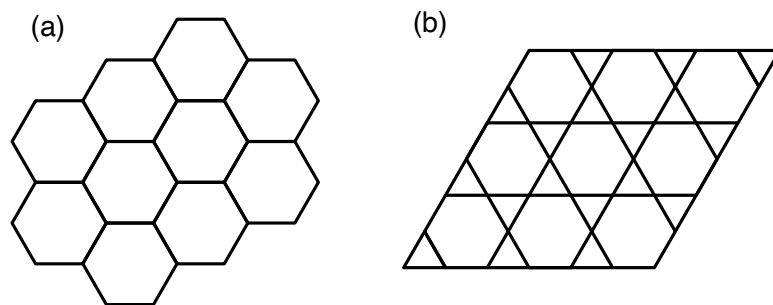


Figure 1.1: An illustration of (a) the honeycomb lattice, the underlying lattice structure of graphene, and (b) the kagome lattice, which is the system of interest in this thesis.

2D materials are intrinsically different than 3D materials. Specifically, they can host novel topological states and give rise to otherwise impossible quantum phases, such as the integer and fractional quantum Hall effect [2, 3], where the Hall conductance is quantized precisely as an integer multiple or fraction multiple of the conductance quantum $\frac{e^2}{h}$, respectively; here, e is the elementary charge, and h is the Planck constant. In addition, 2D crystals containing a transition metal in the unit cell may give rise to many intriguing phenomena, such as superconductivity, charge-density waves (CDW), and spin-density waves (SDW) [4]. For this reason, much emphasis is put towards fully understanding the phases of those quantum materials.

With new methods of engineering 2D materials available, solids consisting of different lattice structures emerge. In addition to graphene, which resembles a honeycomb lattice, a class of materials called the kagome materials [5] are now realizable [6, 7] (See Fig. 1.1 (b)). Kagome materials are specifically interesting as 2D lattice because they can host novel, correlated, electronic phenomena [8, 9, 10, 11, 12, 13, 14]. In particular, Van Hove singularities (VHS), referring to a divergence in the density of states of an electronic band, substantially enhance the interaction effects due to the large accumulation of electronic states around the VHS. These singularities play a crucial role in the emergence of various electronic phenomena in kagome materials, including charge density waves, pair density waves, and unconventional superconductivity [15, 16, 17, 18, 19, 20, 21].

Recently, the appearance of higher-order VHS (HOVHS), which would result in even stronger power-law divergent DOS, has attracted much experimental and theoretical interest as a pathway to explore novel electronic orders [22, 23, 24, 25, 26, 27, 28, 29, 30, 31, 32, 33, 34], specifically in the context of cuprate band structures [35, 36]. In particular, when HOVHS emerge in topological bands, characterized by the Chern number, the interplay between band topology and high DOS can

promote novel electronic orders [37, 38, 39], such as superconducting pair-density waves and Chern supermetals [37]. The importance of combining higher-order singularities and nontrivial band topology is thus emphasized, and such interplay on the kagome lattice remain largely unexplored.

In this thesis, I will investigate the effects of a complex next-nearest-neighbor (NNN) hopping amplitude, $t_2 e^{i\phi}$, on the electronic bands of a kagome lattice. This hopping term, analogous to the Haldane model on the honeycomb lattice [40], breaks time-reversal symmetry (TRS) and induces the formation of bands with nonzero Chern numbers. Employing a systematic analytical and numerical classification of critical points at high-symmetry points Γ , $\pm\mathbf{K}$, and \mathbf{M}_i ($i = 1, 2, 3$) of the Brillouin zone as a function of (t_2, ϕ) , we reveal a rich landscape of HOVHS in this time-reversal broken kagome system. Notably, we identify conditions under which bands with Chern numbers as large as $C = \pm 4$, emerge. Owing to the presence of HOVHSs, these bands support power-law divergences in the DOS, $\rho(\epsilon) \sim |\epsilon|^{-\nu}$, with exponents $\nu = \frac{1}{2}$, $\frac{1}{3}$, and $\frac{1}{4}$. In addition to the classification of HOVHS, this TRS-broken system reveals new features of the kagome band structure:

(1) While the NNN hopping destroys the exact flatness condition of the third band in the nearest-neighbor (NN) kagome lattice [41, 42, 43] (a special case where all points in the Brillouin zone become critical at $t_2 = 0$), our phase diagram uncovers HOVHS lines at the high symmetry points \mathbf{K} and \mathbf{M}_i in the (t_2, ϕ) parameter space, which converge to a flat band at $(t_2 \rightarrow 0, \phi = \pm\pi/2)$. Thus the kagome lattice provides a relevant setting to study the emergence of HOVHS near stronger DOS singularities due to flatbands.

(2) In the lowest band, our classification of HOVHS not only identifies the loci of high DOS but also pinpoints the location of a nearly flat Chern band with $C = \pm 1$ in the (t_2, ϕ) parameter space. This provides an ideal scenario for exploring competing

electronic orders and emergent fractional Chern insulators [44, 45, 46, 47, 48] in a partially filled band.

(3) The NNN chiral hopping, while breaking TRS, preserves the sublattice interference (SI) [8, 49, 50] of the second band for the entire parameter space (t_2, ϕ) . SI implies that electronic states associated with M_i points at the Brillouin zone boundary are maximally localized on the sublattices A, B, and C, which has a non-trivial effect on interactions when the Fermi energy crosses a HOVHS at the M_i points at the zone boundary. Our work thus extends the mechanism of SI in time-reversal broken Chern bands from the Chern number $C = \pm 1$ band on the honeycomb lattice [37] into the realm of topological kagome bands supporting higher Chern numbers, $C = \pm 2$ and $C = \pm 4$.

This work opens a direction to explore exotic kagome bands in synthetic materials such as optical lattices [7]. In particular, an implementation of the complex NNN hopping akin to a Haldane optical lattices [51] could be achieved via periodic modulation using piezoelectric actuators. Moreover, the recent discovery of a new family of kagome metals, AV_3Sb_5 ($A = K, Rb, Cs$) displaying a variety of exotic correlated electronic phenomena [8, 9, 10, 11, 12, 13, 14] and exhibiting both conventional and higher-order Van Hove singularities [6, 52, 53], as evidenced by angle-resolved photoemission spectroscopy (ARPES) [32, 33], further motivates a deeper exploration of the HOVHS landscape in kagome lattices. While kagome systems have been actively studied in connection with Van Hove singularities, the relationship between VHS and non-trivial band topology in these materials remains largely unexplored.

Chapter 2

Background

2.1 Kagome Systems

There are two main methods to investigate the kagome lattice. The first is through natural kagome metals. Examples of this type are AV_3Sb_5 ($A = K, Rb, Cs$) [6], a class of kagome materials displaying a variety of exotic correlated electronic phenomena [8, 9, 10, 11, 12, 13, 14] and exhibiting both conventional and higher-order Van Hove singularities [6, 52, 53], as evidenced by angle-resolved photoemission spectroscopy (ARPES) [32, 33]. Co-based kagome materials, namely $MgCo_6Ge_6$ and $YbCo_6Ge_6$, have also been shown to exhibit higher-order Van Hove singularities [54], confirming that HOVHS indeed can emerge and requires further understanding in those systems.

Another avenue to explore kagome lattice is through optical lattice [55, 56, 57, 58]. As a synthetic material, optical lattice gives experimentalists more freedom to control certain aspects of the system of interest, specifically hopping strength between neighboring sites. The kagome lattice has already been realized on an optical lattice in 2012 [7] and has been intensely studied [59, 60, 61]. Additionally, with theoretical work on realizing complex hopping processes established [62, 63],

the Haldane model was finally realized [51], almost 30 years after the original paper by Haldane [40]. The model which we investigate in this thesis can particularly take advantage of this achievement, since the Hamiltonian also involves a complex, NNN electron hopping process.

2.2 Van Hove Singularities

Leon Van Hove has shown that in 2D lattice systems, saddle points on the electronic bands lead to divergence in the density of states (DOS) [64]. Fig. 2.1 showcases a saddle point on a 2D electronic band, with the low-energy expansion around it as $\epsilon = \epsilon_0 + \alpha(p_x^2 - p_y^2)$. For the rest of this section, the constant ϵ_0 will be omitted. When one calculates the DOS around the energy ϵ_0 , there exists a divergence in the form of logarithmic law, $\rho(\epsilon) \propto \log |\frac{\Lambda}{\epsilon}|$, where $\rho(\epsilon)$ is the DOS as a function of energy ϵ and Λ is the energy cutoff. In the context of condensed matter physics, this singularity in the DOS is referred to as a Van Hove singularity (VHS). In particular, we will refer to the saddle points of the type shown in Fig. 2.1 as conventional saddle points, as there exists higher-order ones, exhibiting power-law divergence.

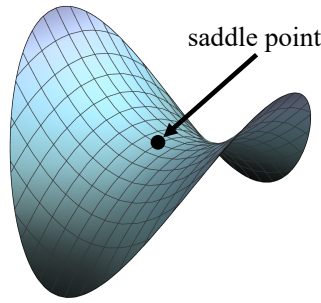


Figure 2.1: A conventional saddle point on a 2-dimensional manifold. The Taylor expansion around the saddle point reads $z \propto x^2 - y^2$.

To mathematically distinguish the conventional saddle points and the higher-order critical points, it is necessary to introduce the mathematical object Hessian, which is defined as $\mathbb{H}_{n,\mathbf{k}} = \det(\frac{\partial^2 \epsilon_{n,\mathbf{k}}}{\partial k_i \partial k_j})$, where $\epsilon_{n,\mathbf{k}}$ is the electronic band in momen-

tum space with band index n and wavevector k . Consider a critical point (i.e. where the gradient is 0, $\nabla_{\mathbf{k}}\epsilon_{n,\mathbf{k}} = 0$) on a 2D Bloch band. We can proceed to expand the dispersion relation around point of interest, ϵ_0 :

$$\epsilon_{k+p} - \epsilon_0 = \alpha p_x^2 + \beta p_y^2 + 2\gamma p_x p_y + \dots, \quad (2.1)$$

where α , β , and γ are all real coefficients. In the basis of k_x and k_y , we can express the second-order terms using matrices:

$$\epsilon_{k+p} - \epsilon_0 = (p_x \ p_y) \begin{pmatrix} \alpha & \gamma \\ \gamma & \beta \end{pmatrix} \begin{pmatrix} p_x \\ p_y \end{pmatrix} \quad (2.2)$$

The determinant of the 2×2 matrix in Eq. (2.2) then is the Hessian quantity mentioned above. Intuitively, as a scalar, Hessian provides information on the second-order curvature at the point of interest. For a conventional saddle point on a Bloch band, the following conditions must be satisfied: $\nabla_{\mathbf{k}}\epsilon_{n,\mathbf{k}} = 0$ and $\mathbb{H}_{n,\mathbf{k}} < 0$. For (conventional) extrema points, the Hessian would instead be $\mathbb{H}_{n,\mathbf{k}} > 0$. Interestingly, a new set of critical points emerges when Hessian vanishes, which form higher-order critical points (they can be either a saddle point or an extremum). Accordingly, this type of points corresponds to a new physical singularity, higher-order Van Hove singularity (HOVHS). HOVHS exhibits a higher power-law divergence in DOS, and these higher-order singularities in kagome systems will remain the focus of the thesis.

2.3 Berry Curvature

Haldane has shown that a 2D lattice system could host topological bands without external magnetic field [40], hence birthing the concept of anomalous integer

quantum Hall effect. Here, the quantity that characterizes the quantized Hall conductance is called the Chern number, a topological invariant of the electronic band of interest. Moreover, Berry curvature is a geometric quantity closely connected with the Chern number, as they are related in the following manner:

$$C_n = \frac{1}{2\pi} \int \Omega(\mathbf{k}) d^2\mathbf{k} = \frac{1}{2\pi} \int \nabla_k \times \mathbf{A}(\mathbf{k}) d^2\mathbf{k}, \quad (2.3)$$

where C_n is the Chern number of band with index n , and $\Omega(\mathbf{k}) = \nabla_k \times \mathbf{A}(\mathbf{k})$ corresponds to the gauge invariant Berry curvature, where $\mathbf{A}(\mathbf{k})$ is called the gauge-dependent Berry connection:

$$\mathbf{A}(\mathbf{k}) = i \langle n(\mathbf{k}) | \frac{\partial}{\partial \mathbf{k}} | n(\mathbf{k}) \rangle \approx \frac{i}{\Delta \mathbf{k}} \langle n(\mathbf{k}) | (|n(\mathbf{k} + \Delta \mathbf{k})\rangle - |n(\mathbf{k})\rangle). \quad (2.4)$$

For the calculations of Chern numbers in Sec. 4.2, we use specifically the Fukui method to numerically compute the Berry curvature of each electronic band [65]. For this method, the 1st Brillouin zone (BZ) would be divided into a $N \times N$ grid of plaquettes. And for each plaquette, the line integral $\oint \mathbf{A} \cdot d\mathbf{k}$ around the plaquette is computed using Eq. (2.4), and it is gauge invariant. The geometric phases for all plaquettes in the 1st BZ are then summed, giving the Chern number of a given band.

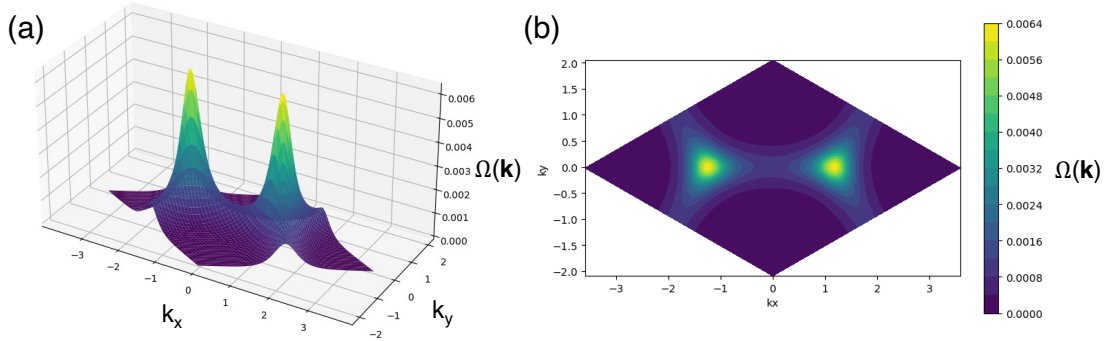


Figure 2.2: Example of Berry curvature using the Fukui method. The Chern number resulting from this curvature is 1.

Chapter 3

Model

We study a tight-binding model of the kagome lattice with lattice constant a , consisting of NN hopping as well as complex NNN hopping,

$$H = -t_1 \sum_{\langle i,j \rangle} c_i^\dagger c_j - t_2 \sum_{\langle\langle i,j \rangle\rangle} e^{i\phi_{ij}} c_i^\dagger c_j + h.c., \quad (3.1)$$

where t_1 (t_2) is the NN (NNN) hopping strength, ϕ_{ij} is the phase factor associated with the NNN hopping between sites i and j , $\langle i, j \rangle$ and $\langle\langle i, j \rangle\rangle$ indicates the NN and NNN hopping respectively, and c_j^\dagger (c_j) is the fermionic creation (annihilation) operator at site j . The vectors connecting the NN atomic sites are defined as $\mathbf{a}_1 = \frac{a}{2}(1, 0)$, $\mathbf{a}_2 = \frac{a}{4}(1, \sqrt{3})$ and $\mathbf{a}_3 = \mathbf{a}_1 - \mathbf{a}_2$, and the NNN hopping vectors are defined as $\mathbf{b}_1 = \frac{a}{2}(0, \sqrt{3})$, $\mathbf{b}_2 = \frac{a}{4}(3, -\sqrt{3})$, and $\mathbf{b}_3 = -(\mathbf{b}_1 + \mathbf{b}_2)$, as shown in Fig. 3.1. Notice that the black dashed arrows shown in Fig. 3.1 denote the direction of the complex NNN hopping. Furthermore, we assume the system is spin-polarized, thereby omitting the spin degree of freedom.

In the momentum space, the Hamiltonian reads $H = \sum_{\mathbf{k}} c_{\mathbf{k}}^\dagger \hat{\mathcal{H}}(\mathbf{k}) c_{\mathbf{k}}$, where $\hat{\mathcal{H}}(\mathbf{k}) = \hat{\mathcal{H}}_{NN}(\mathbf{k}) + \hat{\mathcal{H}}_{NNN}(\mathbf{k})$, and $c_{\mathbf{k}} = (c_{\mathbf{k},A} \ c_{\mathbf{k},B} \ c_{\mathbf{k},C})^T$, with A, B, C being the three sites of the kagome unit cell displayed in Fig. 3.1. The momentum \mathbf{k} is defined in the first Brillouin zone (BZ) spanned by the two reciprocal lattice vectors,

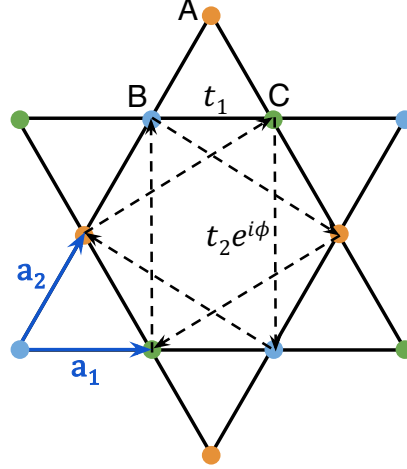


Figure 3.1: Kagome lattice with the sites A, B, and C marked in orange, blue, and green respectively. The vectors connecting site B with its nearest neighbors A and C are denoted as \mathbf{a}_2 and \mathbf{a}_1 respectively. The real NN hopping amplitude, t_1 , is represented by solid black lines. The black dashed arrows show the orientation of the NNN hoppings with strength $t_2 e^{i\phi}$. This NNN hopping breaks time-reversal symmetry while preserving \mathcal{C}_3 rotation and inversion symmetry about the center of the hexagon.

$\mathbf{G}_1 = \frac{2\pi}{a}(1, -\frac{1}{\sqrt{3}})$ and $\mathbf{G}_2 = \frac{2\pi}{a}(0, \frac{2}{\sqrt{3}})$. The lattice constant a will henceforth be set to 1. The single particle Hamiltonian $\hat{\mathcal{H}}(\mathbf{k})$ can be expressed as

$$\hat{\mathcal{H}}(\mathbf{k}) = \begin{pmatrix} 0 & h_{12}(\mathbf{k}) & h_{13}(\mathbf{k}) \\ h_{12}^*(\mathbf{k}) & 0 & h_{23}(\mathbf{k}) \\ h_{13}^*(\mathbf{k}) & h_{23}^*(\mathbf{k}) & 0 \end{pmatrix}, \quad (3.2)$$

where $h_{12}(\mathbf{k}) = -2t_1 \cos(\mathbf{k} \cdot \mathbf{a}_2) - 2t_2 e^{i\phi} \cos(\mathbf{k} \cdot \mathbf{b}_2)$, $h_{13}(\mathbf{k}) = -2t_1 \cos(\mathbf{k} \cdot \mathbf{a}_3) - 2t_2 e^{-i\phi} \cos(\mathbf{k} \cdot \mathbf{b}_3)$, and $h_{23}(\mathbf{k}) = -2t_1 \cos(\mathbf{k} \cdot \mathbf{a}_1) - 2t_2 e^{i\phi} \cos(\mathbf{k} \cdot \mathbf{b}_1)$.

Diagonalization of the Hamiltonian given in Eq. (3.2), $H = \sum_{\mathbf{k}} \sum_{n=1,2,3} \Psi_{n,\mathbf{k}}^\dagger \epsilon_{n,\mathbf{k}} \Psi_{n,\mathbf{k}}$, yields the dispersion of each band, $\epsilon_{n,\mathbf{k}}$, where $n = 1, 2, 3$ denotes the index of the first, second and third energy bands, respectively, in ascending order. Henceforth, energy is expressed in units of t_1 . Owing to \mathcal{C}_3 rotation and inversion symmetries, the spectrum satisfies $\epsilon_{n,\mathcal{C}_3\mathbf{k}} = \epsilon_{n,\mathbf{k}}$ and $\epsilon_{n,-\mathbf{k}} = \epsilon_{n,\mathbf{k}}$.

Chapter 4

Analysis

4.1 Higher-order Van Hove Singularities

In 2D Bloch bands, an ordinary VHS exhibits logarithmic divergence in the DOS ($\rho \propto \log|\epsilon|$) [64], which occurs at a saddle point (i.e., where the dispersion is locally $\epsilon_{n,k} \sim k_x^2 - k_y^2$), with the following conditions satisfied: $\nabla_{\mathbf{k}}\epsilon_{n,\mathbf{k}} = 0$ and $\mathbb{H}_{n,\mathbf{k}} < 0$, where $\mathbb{H}_{n,\mathbf{k}} = \det(\frac{\partial^2\epsilon_{n,\mathbf{k}}}{\partial k_i\partial k_j})$ is the Hessian of the dispersion $\epsilon_{n,\mathbf{k}}$. When the Hessian at a critical point vanishes, the quadratic form approaches degeneracy, making the energy dispersion of at least third order. When this happens, HOVHS emerges with a power-law divergence in DOS [22, 25, 66, 23] due to a higher-order critical point. To clarify the usage of HOVHS in our paper, we point out that this type of singularity can manifest itself in the form of either a higher-order saddle point or a higher-order extrema. While conventional extrema do not give rise to divergence in DOS, higher-order extrema generate a flat local dispersion, inducing a power-law divergence in DOS, which we will discuss in the following subsections. We also emphasize that in the case of an HOVHS resulting from an extremum, we do not observe the emergence of the singularity from the merging of ordinary VHS on the energy band, which is the case in higher-order saddle points like the monkey

saddles [22].

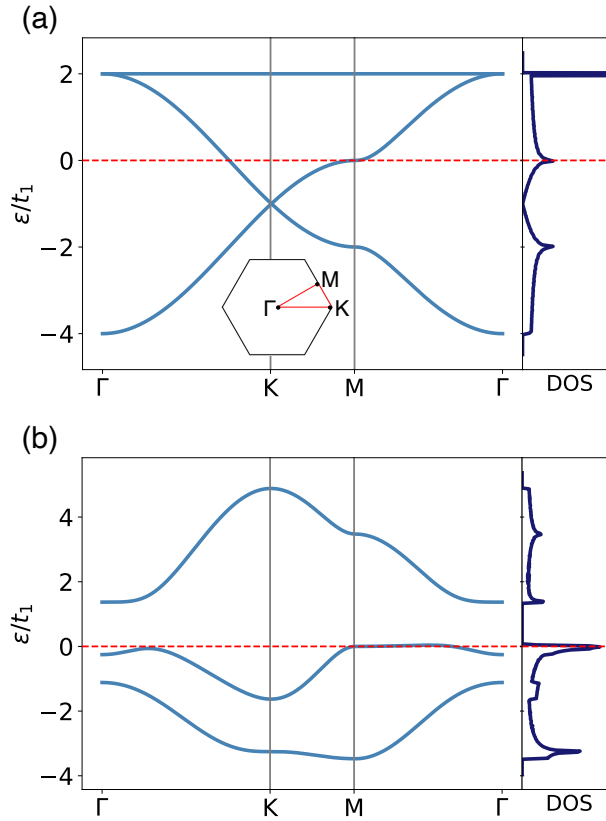


Figure 4.1: Band structure at (a) $(t_2, \phi) = (0, 0)$ and (b) $(t_2, \phi) = (0.76, 0.9\pi)$, with the first BZ shown in (a). The corresponding DOS is displayed on the right. The red dashed lines in (a) and (b) denote the energy at which the M points of the second band support a conventional VHS and a HOVHS respectively, as indicated by the divergences in the corresponding DOS. Notice that the energy corresponding to the M points on band 2 is always zero.

In the absence of NNN hopping, as shown in Fig. 4.1 (a), band 3 is flat and bands 1 and 2 support critical points on the high-symmetry points of the first BZ $\Gamma = (0, 0)$, $\pm\mathbf{K} = (\pm\frac{4\pi}{3}, 0)$, $\mathbf{M}_1 = (\pi, \frac{\pi}{\sqrt{3}})$, $\mathbf{M}_2 = (-\pi, \frac{\pi}{\sqrt{3}})$, and $\mathbf{M}_3 = (0, -\frac{2\pi}{\sqrt{3}})$, with conventional saddle points located on \mathbf{M}_i . Figure 4.1 (b) illustrates the effect of the NNN hopping on the band structure, where we observe the onset of bands with significantly higher DOS divergence than ordinary VHS. Henceforth we focus on addressing how these critical points emerge as a function of the parameters (t_2, ϕ) . As shown below, all high-symmetry points on the three bands can support

HOVHS in this parameter space. In particular, we analyze high-symmetry points separately and classify their HOVHS as shown in Fig. 4.2- 4.4. C_3 rotation and inversion symmetries reduce the analysis to three of the six high-symmetry points.

4.1.1 Critical Points at $\pm\mathbf{K}$

Higher-order singularities emerge at \mathbf{K} in the form of monkey saddles, as shown in Fig. 4.2. The corresponding low-energy dispersion, which reflects the C_3 rotation symmetry around the \mathbf{K} points, takes the form

$$\epsilon_{\mathbf{K}+\mathbf{p}} - \epsilon_{\mathbf{K}} = \alpha(p_x^3 - 3p_x p_y^2) + \dots, \quad (4.1)$$

where p_x and p_y are defined parallel and perpendicular to the $\Gamma\mathbf{K}$ line in the first Brillouin zone, respectively, and the coefficient α is real. This monkey saddle dispersion indicates that the corresponding DOS exhibits a power-law divergence with exponent $\nu = 1/3$ [23, 66, 67, 22], which we confirm numerically. Furthermore, these observations apply to the $-\mathbf{K}$ points as well, since the model is symmetric under inversion.

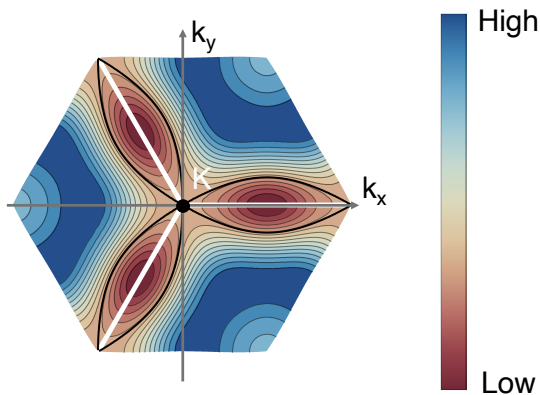


Figure 4.2: Contour plots of the energy dispersion corresponding to band 2, near the high-symmetry point $\pm\mathbf{K}$. The white lines denote the boundaries of the first BZ and the black lines correspond to the Fermi surface contour at the corresponding energy of the HOVHS. The dispersion here exhibits a monkey-saddle dispersion.

4.1.2 Critical Points at Γ

In contrast to the $\pm K$ points, the Γ point does not support a high-order saddle even though the Hessian $\mathbb{H}_{n,\Gamma}$ vanishes. Instead, as the second-order curvature of the dispersion vanishes along both the k_x and k_y directions, Γ becomes an extremum with vanishing Hessian, thereby resulting in a locally flat band around the Γ point, as shown in Fig. 4.3. The corresponding low-energy dispersion takes the form,

$$\epsilon_{\Gamma+\mathbf{p}} - \epsilon_{\Gamma} = \alpha(p_x^2 + p_y^2)^2 = \alpha p^4, \quad (4.2)$$

where α is a real parameter and $(p_x, p_y) = p(\cos\theta, \sin\theta)$. Furthermore, the dispersion exhibits a stronger power-law divergence with exponent $\nu = 1/2$, i.e., $\rho(\epsilon) \propto |\epsilon - \epsilon_{\Gamma}|^{-\frac{1}{2}}$.

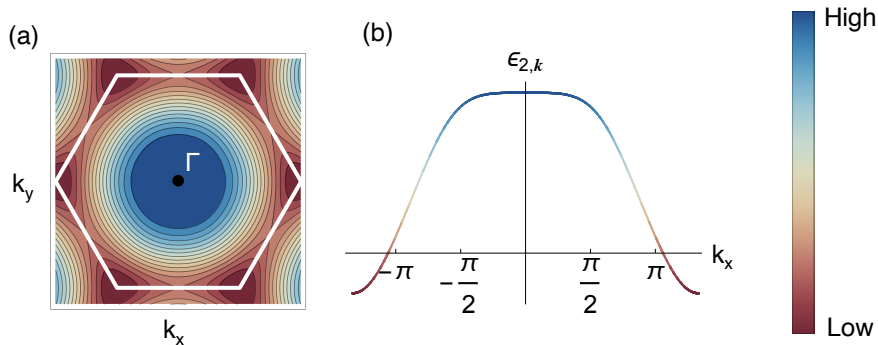


Figure 4.3: Contour plots of the energy dispersion corresponding to band 2, near the high-symmetry point Γ where the Hessian vanishes, thereby supporting HOVHS. At the Γ point (a), which is an extremum, the second-order curvature of the dispersion vanishes along both k_x and k_y directions. (b) The energy dispersion considered in (a), around the Γ point, plotted along k_x with k_y held constant at zero, in order to highlight the flatness of the band around the Γ point.

Additionally, we notice one particular instance at $(t_2, \phi) = (1/3, \pi)$ for the first band where the coefficient α vanishes resulting in a low-energy dispersion of the

form (up to $\mathcal{O}(p^6)$)

$$\epsilon_{\Gamma+\mathbf{p}} - \epsilon_{\Gamma} \approx \frac{p_x^6}{1152} - \frac{p_x^4 p_y^2}{192} + \frac{p_x^2 p_y^4}{128} = \frac{p^6}{1152} \cos^2(3\theta), \quad (4.3)$$

where $\epsilon_{\Gamma} = -\frac{8}{3}$, and the corresponding DOS diverges around Γ as $\rho(\epsilon) \sim |\epsilon - \epsilon_{\Gamma}|^{-2/3}$. We note that both expressions Eqs. (4.2) and (4.3) obey inversion and \mathcal{C}_3 rotation symmetries.

4.1.3 Critical Points at M_i

The emergence of HOVHS at M_i points occurs under two conditions: when either one or both of the eigenvalues of the Hessian \mathbb{H}_{n,M_i} vanish. Given the model has \mathcal{C}_3 symmetry, the following discussion applies to all the M_i points, and hence we drop the subscript i for the M_i points. When one eigenvalue vanishes, the second-order curvature of the dispersion vanishes along either the k_x or k_y direction, resulting in a locally flat band structure in that direction, as shown in Fig. 4.4. The corresponding low-energy dispersion takes the form,

$$\epsilon_{\mathbf{M}+\mathbf{p}} - \epsilon_{\mathbf{M}} = \begin{cases} \alpha p_x^2 + \beta p_x^4 + \gamma p_x^2 p_y^2 + \delta p_y^4 + \dots, & \partial_{k_y}^2 \epsilon_{n,\mathbf{M}} = 0 \\ \alpha p_y^2 + \beta p_x^4 + \gamma p_x^2 p_y^2 + \delta p_x^4 + \dots, & \partial_{k_x}^2 \epsilon_{n,\mathbf{M}} = 0 \end{cases}, \quad (4.4)$$

with all coefficients being real, where the DOS diverges around M as $\rho(\epsilon) \sim |\epsilon - \epsilon_M|^{-1/4}$. On the other hand, when both eigenvalues vanish, the α coefficient vanishes, leading to a fourth-order dispersion in momentum, where the DOS obeys a power-law divergence with exponent $\nu = 1/2$, similar to the case of the Γ point. Here, the second-order curvature vanishes in all directions, making the dispersion at M_i locally flat.

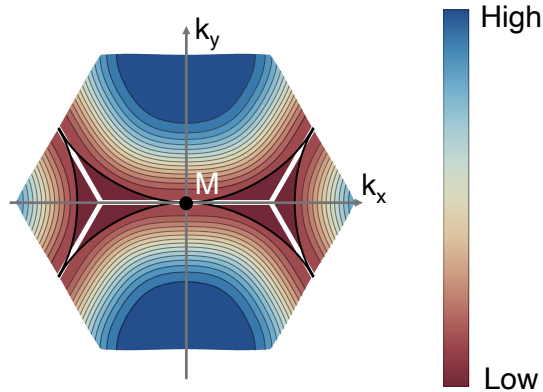


Figure 4.4: Contour plots of the energy dispersion corresponding to band 2, near the high-symmetry point M_i where the Hessian vanishes, thereby supporting HOVHS. Around the M_3 point, the dispersion becomes locally flat only along the k_x direction.

4.1.4 HOVHS Phase Diagrams

We numerically calculate the Hessian for the band dispersions corresponding to the Hamiltonian in Eq. (3.2) around the high-symmetry points $\pm\mathbf{K}$, Γ , and M . Our analysis reveals a range of (t_2, ϕ) values, shown in Fig. 4.5 (a)-(c), for which all three bands support HOVHS at one or more of these high-symmetry points. The critical points marked by the HOVHS lines in Figs. 4.5 (a)-(c) all correspond to a vanishing Hessian. Dashed lines indicate higher-order saddle points, while solid lines denote higher-order extrema. Notice that the higher-order critical point at Γ is invariably an extremum, whereas those at $\pm\mathbf{K}$ are consistently higher-order saddles. Additionally, we find that the Hessian is invariant under the transformation $\phi \rightarrow -\phi$. As a result, we display the HOVHS lines for only $0 \leq \phi \leq \pi$.

We wish to point out an interesting feature of the flat band in Fig. 4.5 (c). As t_2 approaches 0 around $\phi = \pm\pi/2$, two HOVHS lines of M_i and one of $\pm\mathbf{K}$ are seen merging at a single parameter value. This convergence suggests that, as we perturb the system away from $t_2 = 0$ around $\phi = \pm\pi/2$, even when the global band dispersion is no longer perfectly flat, the local energy dispersion around the $\pm\mathbf{K}$ and M_i points remains relatively flat. This provides a unique setting to investigate

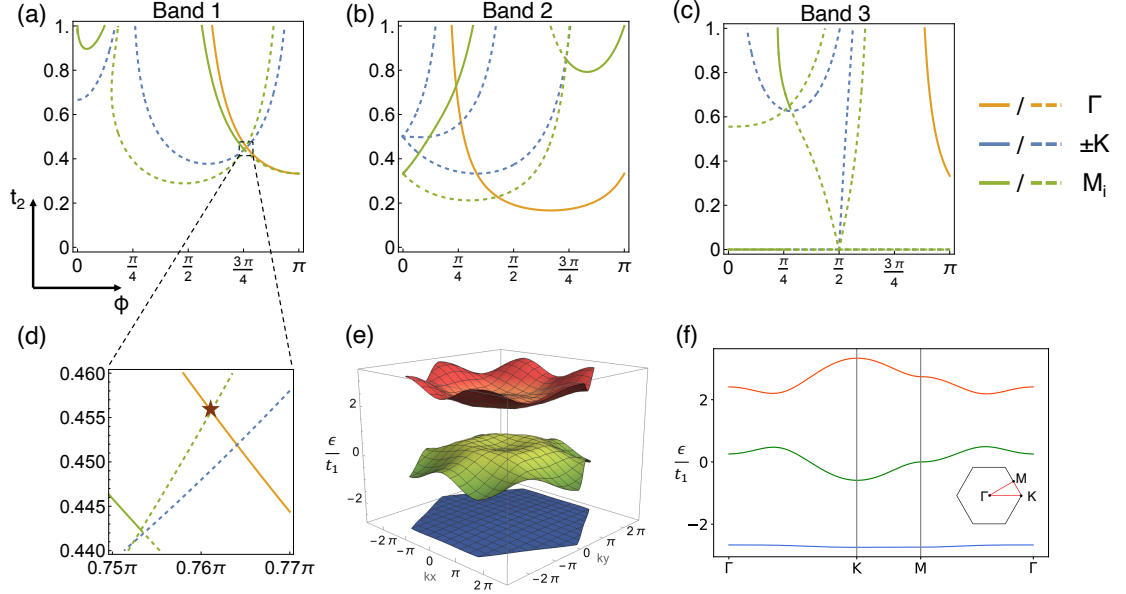


Figure 4.5: (a)-(c) Parameter space plots showing the set of (t_2, ϕ) values for which the high-symmetry points Γ (orange), $\pm K$ (blue) and M (green) corresponding to the bands 1-3 (from left to right) support HOVHSs. The dashed lines correspond to the high-symmetry points which can be classified as higher-order saddles whereas the solid lines correspond to extrema with vanishing Hessian. (d) Parameter space plot zoomed in around the intersections of the lines highlighted with the black dashed lines in (a), clarifying the different intersections of boundary lines. The parameter pair of interest is labeled with \star , with values $(t_2 = 0.45, \phi = 0.76\pi)$. (e) The 3D plot of the band structure at parameters labeled with \star in (d), supporting HOVHSs at both M and Γ points. The energy value corresponding to the HOVHS at the M and Γ points are $-2.74 t_1$ and $-2.67 t_1$ respectively. (f) Band diagram of the same bands to showcase the exceptional flatness of band 1, with an approximate bandwidth of $0.08 t_1$. The first BZ is shown in the diagram as well.

the emergence of HOVHS near stronger DOS singularities due to flat bands.

Additionally, we notice a region in Fig. 4.5 (a) where numerous line intersections occur, for the first band. That region is zoomed in and shown in Fig. 4.5 (d). Coincidentally, the bandwidth in that region also achieves a minimum as low as $\approx 0.08 t_1$. Selecting a parameter pair of $(t_2 = 0.45, \phi = 0.76\pi)$, which is marked with \star in Fig. 4.5 (d), we obtain a band 1 giving rise to HOVHSs both at Γ and M points. The 3D plot of the band structure is showcased in Fig. 4.5 (e), and the 1D band structure of the system is demonstrated in Fig. 4.5 (f), exhibiting the extreme

flatness of the lowest band. The particular region shown in Fig. 4.5 (d) can be a promising territory to observe strongly correlated phenomena in the system.

We now discuss an analytic approach underlying the phase diagrams shown in Figs. 4.5 (a)-(c). In particular, we perturbatively determine the quadratic form near each high-symmetry point. For concreteness, we focus on the Γ point, where nondegenerate perturbation theory holds, except when degeneracies occur between bands 2 and 3 at $\phi = 0, \pi$. Expanding the Hamiltonian about Γ , we get

$$\hat{\mathcal{H}}(\Gamma + \mathbf{p}) = \hat{\mathcal{H}}(\Gamma) + \hat{\mathcal{H}}(\mathbf{p}), \quad (4.5)$$

$$\hat{\mathcal{H}}(\mathbf{p}) = \begin{pmatrix} 0 & \zeta_{12}(\mathbf{p}) & \zeta_{13}(\mathbf{p}) \\ \zeta_{12}^*(\mathbf{p}) & 0 & \zeta_{23}(\mathbf{p}) \\ \zeta_{13}^*(\mathbf{p}) & \zeta_{23}^*(\mathbf{p}) & 0 \end{pmatrix}, \quad (4.6)$$

where, up to second order in momentum, $\zeta_{12} = t_1(\mathbf{p} \cdot \mathbf{a}_2)^2 + t_2 e^{i\phi}(\mathbf{p} \cdot \mathbf{b}_2)^2$, $\zeta_{13} = t_1(\mathbf{p} \cdot \mathbf{a}_3)^2 + t_2 e^{-i\phi}(\mathbf{p} \cdot \mathbf{b}_3)^2$, $\zeta_{23} = t_1(\mathbf{p} \cdot \mathbf{a}_1)^2 + t_2 e^{i\phi}(\mathbf{p} \cdot \mathbf{b}_1)^2$. The eigenstates of $\hat{\mathcal{H}}(\Gamma)$ can be expressed as, $\Psi_{1,\Gamma}^{(0)} = \frac{1}{\sqrt{3}}(1, 1, 1)$, $\Psi_{2,\Gamma}^{(0)} = \left(\frac{1}{6}(-\sqrt{3} - 3i), \frac{1}{6}(-\sqrt{3} + 3i), \frac{1}{\sqrt{3}}\right)$, and $\Psi_{3,\Gamma}^{(0)} = \left(\frac{1}{6}(-\sqrt{3} + 3i), \frac{1}{6}(-\sqrt{3} - 3i), \frac{1}{\sqrt{3}}\right)$.

The dispersion, to leading quadratic order, follows from

$$\epsilon_{n,\Gamma+\mathbf{p}} = \epsilon_{n,\Gamma}^{(0)} + \Psi_{n,\Gamma}^{(0)*} \hat{\mathcal{H}}(\mathbf{p}) \Psi_{n,\Gamma}^{(0)}. \quad (4.7)$$

and, hence, the Hessian $\mathbb{H}_{n,\Gamma}(t_2, \phi)$ of each band:

$$\begin{aligned} \mathbb{H}_{1,\Gamma} &= \left[\frac{3}{4} (t_1 + 3t_2 \cos(\phi)) \right]^2, \\ \mathbb{H}_{2,\Gamma} &= \left[-\frac{1}{8} t_1 \left(1 + 3t_2 \cos(\phi) - 3\sqrt{3}t_2 \sin(\phi) \right) \right]^2, \\ \mathbb{H}_{3,\Gamma} &= \left[-\frac{1}{8} t_1 \left(1 + 3t_2 \cos(\phi) + 3\sqrt{3}t_2 \sin(\phi) \right) \right]^2. \end{aligned} \quad (4.8)$$

Setting $\mathbb{H}_{n,\Gamma} = 0$, results in the HOVHS contours at Γ shown in Fig. 4.5 (orange lines),

$$\begin{aligned}\tau_{1,\Gamma}(\phi) &= -\frac{\sec(\phi)}{3}, \\ \tau_{2,\Gamma}(\phi) &= -\frac{1}{3(\cos(\phi) - \sqrt{3}\sin(\phi))}, \\ \tau_{3,\Gamma}(\phi) &= -\frac{1}{3(\cos(\phi) + \sqrt{3}\sin(\phi))}.\end{aligned}\tag{4.9}$$

The other high-symmetry points can be dealt with similarly. In particular, the analysis of degenerate perturbation theory for Γ at $\phi = \pi$, as well as the Hessian expressions for M and K points are provided in Appendix. A.

4.2 Band Topology

The NNN hopping breaks time-reversal symmetry and leads to the possibility of energy-isolated topological bands characterized by a nonzero Chern number. To investigate that, we numerically compute [65] the Chern number of the three bands in the $t_2 - \phi$ parameter space.

The Chern number diagrams are presented in Fig. 4.6. We restrict our analysis to $0 \leq t_2 \leq 1$ where the magnitude of the second neighbor hopping is less than the NN hopping t_1 . Furthermore, the parameter ϕ is restricted from $[0, \pi]$, since for any Chern number C at (t_2, ϕ) , as ϕ goes to $-\phi$, the Chern number flips sign. The white regions describe bands that are not separated by a direct gap. The colored regions represent isolated bands with nonzero Chern numbers. In this parameter regime, we observe a rich landscape of gapped topological bands, some of which support relatively large Chern numbers.

By combining the phase diagrams shown in Fig. 4.5 and Fig. 4.6, we uncover a comprehensive understanding of how the NNN hopping leads to the onset of

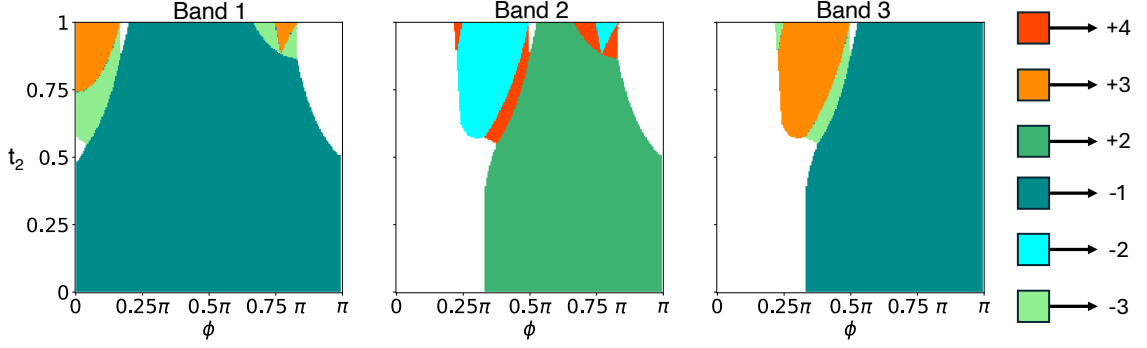


Figure 4.6: Phase diagrams for band 1 (left), band 2 (middle), and band 3 (right), showing the corresponding Chern numbers in the t_2 - ϕ parameter space. Since TRS is respected at $\phi = 0, \pi$, the Chern number for all three bands at $\phi = 0, \pi$ are 0. White regions in the phase diagrams indicate non-positive indirect energy gaps where the Chern number is not well-defined. (In this case, there is no situation where the Fermi energy lies in between the bands, and the bands are characterized by a possible non-quantized anomalous Hall response.) Only $[0, \pi]$ is shown on the ϕ axis, since for any Chern number C at (t_2, ϕ) , as ϕ goes to $-\phi$, the Chern number flips sign. As seen in certain regions of the parameter space, band 2 can support Chern number as high as ± 4 .

topological bands supporting HOVHS at the high-symmetry points, characterized by power-law diverging DOS $\rho(\epsilon) \sim |\epsilon - \epsilon_0|^{-\nu}$, with exponents $\nu = 1/2, 1/4, 1/3$, which is one of the main results of our analysis.

This structure of HOVHS can be accessed upon changing the Fermi energy in each of the bands, which also changes the anomalous Hall response owing to the presence of a finite Berry curvature in the bands. Importantly, the zero temperature differential anomalous Hall response displays a strong divergence whenever the Fermi level crosses a Van Hove singularity, due to the large change in the number of electronic states in a small energy window. At zero-temperature, this response, $\frac{d\sigma_{xy}^{\text{int}}(\mu; T=0)}{d\mu}$, near VHSs can be expressed in terms of the density of states $\rho(\mu)$ as [39]

$$\frac{d\sigma_{xy}^{\text{int}}(\mu; T = 0)}{d\mu} = \frac{e^2}{2\pi h} \langle \Omega \rangle_{FS} \rho(\mu), \quad (4.10)$$

where $\sigma_{xy}^{\text{int}}(\mu; T = 0) = \frac{e^2}{h} \frac{1}{2\pi} \int d^2\mathbf{k} \Omega(\mathbf{k}) \Theta(\mu - \epsilon(\mathbf{k}))$ is the anomalous Hall conductivity at zero-temperature, defined in terms of the Berry curvature $\Omega(\mathbf{k})$, and

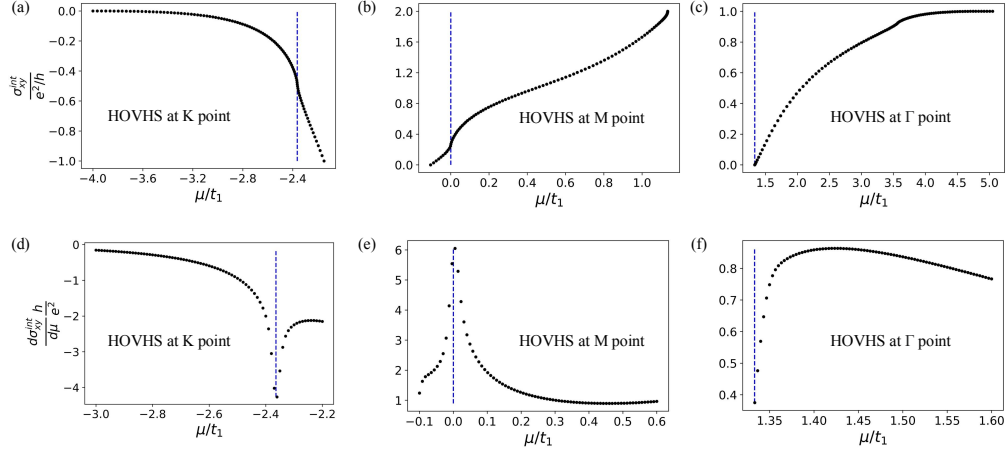


Figure 4.7: (a-c) Intrinsic anomalous Hall conductivity $\sigma_{xy}^{\text{int}}(\mu; 0)$ and (d-f) the corresponding differential anomalous Hall conductivity $\frac{d\sigma_{xy}^{\text{int}}(\mu; 0)}{d\mu}$ at zero temperature, plotted as a function of the Fermi energy μ in units of t_1 for the Chern bands supporting HOVHS at $(t_2, \phi) = (0.39, \pi/2)$ for band 1 (left), $(t_2, \phi) = (0.26, \pi/2)$ for band 2 (middle) and $(t_2, \phi) = (0.80, -0.9\pi)$ for band 3 (right). The high-symmetry point where the HOVHS is located is mentioned in each plot. The differential anomalous Hall response, like the corresponding DOS, exhibits a power-law divergence around μ^* (marked by the blue dashed line) with exponents $1/3$, $1/4$ and $1/2$ for K , M and Γ point respectively.

$\langle \Omega \rangle_{FS}$ defines the average of the Berry curvature on the Fermi surface.

In Fig. 4.7, we plot $\sigma_{xy}^{\text{int}}(\mu; 0)$ as well as $\frac{d\sigma_{xy}^{\text{int}}(\mu; 0)}{d\mu}$ as a function of the Fermi energy μ for three different cases where a Chern band supports HOVHS at either of the three high-symmetry points. Notice that in all the three cases, the inverse of the slope of the anomalous Hall response $\sigma_{xy}^{\text{int}}(\mu; 0)$ vanishes as $\mu \rightarrow \mu^*$ where μ^* is the energy corresponding to the HOVHS, shown in Figs. 4.7 (a)-(c). As a result, the $\frac{d\sigma_{xy}^{\text{int}}(\mu; 0)}{d\mu}$ plots show a divergence as $\mu \rightarrow \mu^*$, displayed in Figs. 4.7 (d)-(f).

We numerically confirm that the differential anomalous Hall responses exhibit power-law divergences with the same exponent as the corresponding DOS, and note that the distinctly sharp peaks become progressively broadened as temperature increases.

4.3 Sublattice Interference

A remarkable feature of Kagome systems is that Bloch states of the second band corresponding to each M_i point in the Brillouin zone are maximally localized on one of the three sublattices A, B and C. Notably, this form of sublattice interference (SI) [8, 49, 17] is persistent even with long-range real hopping terms extending up to the third nearest neighbor [49]. However, SI in kagome systems supporting topological bands is yet to be explored. In this section, we investigate the rich interplay between SI and HOVHS promoted by the complex hopping.

First, we establish that the SI *persists on band 2 throughout the t_2 - ϕ parameter space*. For instance, consider the high-symmetry point $M_1 = (\pi, \frac{\pi}{\sqrt{3}})$. Working out the dot product of M_1 with the lattice vectors a_i and b_i , $M_1 \cdot a_1 = \pi/2$, $M_1 \cdot a_2 = \pi/2$, $M_1 \cdot a_3 = 0$, $M_1 \cdot b_1 = \pi/2$, $M_1 \cdot b_2 = \pi/2$ and $M_1 \cdot b_3 = -\pi$, yields the Hamiltonian $\hat{H}(M_1)$

$$\hat{H}(M_1) = -2t_1 \begin{pmatrix} 0 & 0 & 1 \\ 0 & 0 & 0 \\ 1 & 0 & 0 \end{pmatrix} - 2t_2 \begin{pmatrix} 0 & 0 & -e^{i\phi} \\ 0 & 0 & 0 \\ -e^{-i\phi} & 0 & 0 \end{pmatrix}, \quad (4.11)$$

supporting the energy values, $\epsilon_{1,3} = \pm 2\sqrt{(t_1 - t_2 e^{-i\phi})(t_1 - t_2 e^{i\phi})}$ and $\epsilon_2 = 0$, where $\epsilon_1 \leq \epsilon_2 \leq \epsilon_3$. The corresponding eigenstates are denoted as $\Psi_{n,\mathbf{k}} = u_{\lambda,\mathbf{k}} c_{\mathbf{k}}$, where $u_{\lambda,\mathbf{k}}$ is a unitary transformation with $\lambda = A, B, C$. Notably, the $\epsilon = 0$ case corresponds to the second band with eigenvector $\Psi_{2,M_1} = (0\ 1\ 0)^T$, localized on the B sublattice.

Similarly, for the other two high-symmetry points M_2 and M_3 , the eigenvalues of the corresponding Hamiltonian yield the eigenvalues $\epsilon_1 \leq \epsilon_2 = 0 \leq \epsilon_3$, where the $\epsilon = 0$ case again corresponds to the second band. Owing to \mathcal{C}_3 rotation symmetry, the eigenvectors of the second band at M_2 and M_3 , $\Psi_{2,M_2} = (0\ 0\ 1)^T$ and $\Psi_{2,M_3} =$

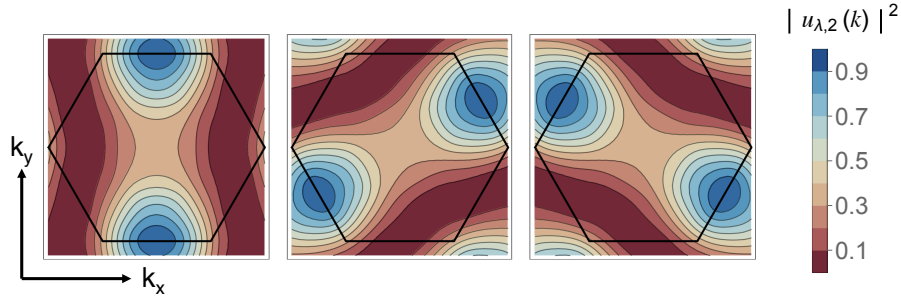


Figure 4.8: Contour plot of the sublattice weights for the second band corresponding to the sites A (left), B (middle), and C (right) of the kagome lattice at $(t_2, \phi) = (0.258, \pi/2)$, demonstrating that each M_i point on band 2 corresponds to one of the three sites of the kagome lattice. In this example, the band carries a Chern number of +2 while supporting HOVHS at the M points. Here, the black lines denote the first Brillouin zone boundaries.

$(1\ 0\ 0)^T$, are maximally localized on the C and A sublattices, respectively. Fig. 4.8 shows the strong sublattice localization at each of M_i on the second band.

SI plays an important role in constraining the interactions between electronic states located near M_i when the Fermi level crosses a Van Hove singularity. Earlier works have explored this regime for logarithmic VHS in kagome lattice [8, 49, 17]. The presence of the complex hopping on this kagome lattice, remarkably, uncovers a new regime where the second band supports HOVHS on the M_i , displayed in the green contours of Fig. 4.5. Furthermore, these band support higher Chern numbers, $C = \pm 2, \pm 4$ (middle panel of Fig. 4.6), generalizing the SI in time-reversal broken Chern bands beyond the Chern number $C = \pm 1$ band on the honeycomb lattice [37]. The identification of topological bands showing SI and HOVHS is a promising platform to explore electronic correlations.

Chapter 5

Conclusion

Motivated by recent interest in band structures supporting higher-order Van Hove singularities, we have investigated a kagome system characterized by NN and NNN hopping, which, respectively, preserve and break time-reversal symmetry (Fig. 3.1). The latter, similarly, to a chiral hopping on the Haldane lattice, leads to the formation of topological bands supporting Chern numbers $C = \pm 1, \pm 2, \pm 3, \pm 4$, as depicted in Fig. 4.6.

More notably, we have performed a comprehensive analytical and numerical analysis of the band dispersions near the six high-symmetry points Γ , $\pm K$, and M_i ($i = 1, 2, 3$), which uncovered a complex and diverse domain of HOVHS controlled by the magnitude and phase of the NNN hopping (Figs. 4.1-4.5). As such, our analysis unveils Chern bands with strong power law divergence in the DOS, $\rho(\epsilon) \sim |\epsilon|^{-\nu}$ characterized by the exponents $\nu = 1/2, 1/3, 1/4$. Such strong singularities in the density of states can imprint characteristic features in the low temperature intrinsic anomalous Hall response, when the Fermi level crosses the HOVHS (Fig. 4.7).

We have explored distinct features of the kagome system worth mentioning. First, while it takes a critical value of the NNN hopping strength for HOVHS to emerge in bands 1 and 2, HOVHS can emerge at the $\pm K$ and M_i out of the third

(flat) band for infinitesimal strength of the NNN, as shown in Fig. 4.5. Furthermore, the NNN hopping provides a mechanism for the realization of high Chern number bands manifesting a sublattice interference whereupon electronic states of the second band are maximally localized on the A, B, and C sublattices as the momentum approaches M_3 , M_1 , and M_2 , respectively (Fig. 4.8).

The classification of HOVHS in kagome systems opens promising directions for future investigation. In particular, the interplay between band topology and large density of states provides a guiding principle to exploring correlation effects in kagome lattices, which could serve as a mechanism to realize unconventional electronic orders such as chiral topological superconductivity and fractional topological states. Another interesting direction to explore would be incorporating a spin degree of freedom into our model, which can be experimentally realized in kagome FeGe metals [68, 69, 70].

Appendix A

Analytical Expressions of the HOVHS

Lines

On the line $\phi = \pi$ in the t_2 - ϕ parameter space, bands 2 and 3 are touching at Γ point, and thus need the degenerate perturbation theory (PT) treatment. We can set up the matrix

$$V = \begin{pmatrix} V_{22} & V_{23} \\ V_{23}^* & V_{33} \end{pmatrix}, \quad (\text{A.1})$$

where $V_{ij} = \Psi_{i,\Gamma}^{(0)*} \hat{\mathcal{H}}(\mathbf{p}) \Psi_{j,\Gamma}^{(0)}$. After diagonalization, we use the two eigenvalues, $3t_2/4$ and $-1/4$, in replacement of $\Psi_{n,\Gamma}^{(0)*} \hat{\mathcal{H}}(\mathbf{p}) \Psi_{n,\Gamma}^{(0)}$ for the energy shift in Eq. (4.7).

Given that the perturbation matrices for M and K have both linear and quadratic dependence on \mathbf{p} , we use second order perturbation theory, with the energy shift defined as the following:

$$\epsilon_{n,k+\mathbf{p}} - \epsilon_{n,k}^{(0)} = \hat{\mathcal{H}}_{nn}(\mathbf{p}) + \sum_{m \neq n} \frac{|\hat{\mathcal{H}}_{nm}(\mathbf{p})|^2}{\epsilon_{n,k}^{(0)} - \epsilon_{m,k}^{(0)}}, \quad (\text{A.2})$$

where k can be K or M , and $\hat{\mathcal{H}}_{nm} \equiv \Psi_{n,k}^{(0)*} \hat{\mathcal{H}}(\mathbf{p}) \Psi_{m,k}^{(0)}$. With Eq. (A.2), we derived the expressions for Hessian at M and $\pm K$ points:

$$\begin{aligned}
\mathbb{H}_{1,\mathcal{M}}(t_2, \phi) &= \frac{1}{64\gamma^6} \\
&\times 3 \left(\gamma - 9t_2^4 - 9\gamma t_2^3 \cos(3\phi) + (15\gamma - 4)t_2^2 \cos(2\phi) + t_2 \left(-7\gamma + 22t_2^2 + 2 \right) \cos(\phi) - 12t_2^2 + 1 \right) \\
&\times \left(-\gamma + t_2^4 + t_2 \left(-(\gamma + 6t_2^2 + 2) \cos(\phi) + \gamma t_2 (t_2 \cos(3\phi) + \cos(2\phi)) + 8t_2 \cos^2(\phi) \right) - 1 \right)
\end{aligned} \tag{A.3}$$

$$\begin{aligned}
\mathbb{H}_{2,\mathcal{M}}(t_2, \phi) &= \frac{1}{16\gamma^4} \\
&\times \left(9t_2^3 \cos(3\phi) - 15t_2^2 \cos(2\phi) + 7t_2 \cos(\phi) - 1 \right) \left(-3t_2^2 (t_2 \cos(3\phi) + \cos(2\phi)) + 3t_2 \cos(\phi) + 3 \right)
\end{aligned} \tag{A.4}$$

$$\begin{aligned}
\mathbb{H}_{3,\mathcal{M}}(t_2, \phi) &= \frac{1}{64\gamma^6} \\
&\times \left(9t_2^4 + \gamma \left(1 - 9t_2^3 \cos(3\phi) \right) + (15\gamma + 4)t_2^2 \cos(2\phi) - t_2 \left(7\gamma + 22t_2^2 + 2 \right) \cos(\phi) + 12t_2^2 - 1 \right) \\
&\times \left(3t_2 \left(\left(-\gamma + 6t_2^2 + 2 \right) \cos(\phi) + \gamma t_2 (t_2 \cos(3\phi) + \cos(2\phi)) - 8t_2 \cos^2(\phi) \right) - 3 \left(\gamma + t_2^4 - 1 \right) \right)
\end{aligned} \tag{A.5}$$

$$\begin{aligned}
\mathbb{H}_{1,\pm\mathcal{K}}(t_2, \phi) &= \frac{1}{16t_2 \left(-6t_2 \cot(\phi) + 2\sqrt{3}t_2 + 3 \csc(\phi) \right)} \csc(\phi) \\
&\times \left(36t_2^3 - 24t_2^2 \cos(\phi) + \sqrt{3} \left(4t_2^2 \sin(\phi) (5 - 12t_2 \cos(\phi)) + 6t_2 \cot(\phi) - 3 \csc(\phi) \right) - 6t_2 \right)
\end{aligned} \tag{A.6}$$

$$\begin{aligned}
\mathbb{H}_{2,\pm\mathcal{K}}(t_2, \phi) &= \frac{1}{16t_2 \left(6t_2 \cot(\phi) + 2\sqrt{3}t_2 - 3 \csc(\phi) \right)} \csc(\phi) \\
&\times \left(-36t_2^3 + 24t_2^2 \cos(\phi) + \sqrt{3} \left(4t_2^2 \sin(\phi) (5 - 12t_2 \cos(\phi)) + 6t_2 \cot(\phi) - 3 \csc(\phi) \right) + 6t_2 \right)
\end{aligned} \tag{A.7}$$

$$\mathbb{H}_{3,\pm K}(t_2, \phi) = \frac{1}{8} \left(\frac{3 - 6t_2 \cos(\phi)}{8t_2^2 \cos(2\phi) + 4t_2^2 - 12t_2 \cos(\phi) + 3} + 6t_2 \cos(\phi) - 1 \right), \quad (\text{A.8})$$

where $\gamma = \sqrt{t_2^2 - 2t_2 \cos(\phi) + 1}$. At specific (t_2, ϕ) values in the parameter space, the $\pm K$ points on either pair of neighboring bands will touch. Due to the no-level crossing theorem under the PT framework, we want to emphasize the $\mathbb{H}_{n,K}$ expressions are only valid in some regions of the parameter space. The band-crossing happens at a set of (t_2, ϕ) values, related by the function $t_2 = \frac{3}{2(\sqrt{3} \sin(\phi) + 3 \cos(\phi))}$. Starting from the NN kagome model, i.e., $(t_2, \phi) = (0, 0)$, once the critical (t_2, ϕ) line is crossed, the Hessian expressions for $\pm K$, as given in Eqs.(A.6)-(A.8), become mixed and do not correspond to the correct band index n . However, we wish to point out that upon plotting the roots of all three $\mathbb{H}_{n,\pm K}$ expressions, we do obtain the complete set of HOVHS lines for the $\pm K$ points in the parameter space.

Bibliography

- [1] Kostya S Novoselov, Andre K Geim, Sergei V Morozov, De-eng Jiang, Yanshui Zhang, Sergey V Dubonos, Irina V Grigorieva, and Alexandr A Firsov. Electric field effect in atomically thin carbon films. *Science*, 306(5696):666–669, 2004.
- [2] Klaus Von Klitzing. The quantized hall effect. *Reviews of Modern Physics*, 58(3):519, 1986.
- [3] Marvin E Cage, Kv Klitzing, AM Chang, F Duncan, M Haldane, Robert B Laughlin, AMM Pruisken, and DJ Thouless. *The quantum Hall effect*. Springer Science & Business Media, 2012.
- [4] K S Novoselov, Artem Mishchenko, Alexandra Carvalho, and AH Castro Neto. 2d materials and van der waals heterostructures. *Science*, 353(6298):aac9439, 2016.
- [5] Itiro Syôzi. Statistics of kagomé lattice. *Progress of Theoretical Physics*, 6(3):306–308, 1951.
- [6] Brenden R Ortiz, Lídia C Gomes, Jennifer R Morey, Michal Winiarski, Mitchell Bordelon, John S Mangum, Iain WH Oswald, Jose A Rodriguez-Rivera, James R

- Neilson, Stephen D Wilson, et al. New kagome prototype materials: discovery of KV_3Sb_5 , RbV_3Sb_5 , and CsV_3Sb_5 . *Physical Review Materials*, 3(9):094407, 2019.
- [7] Gyu-Boong Jo, Jennie Guzman, Claire K Thomas, Pavan Hosur, Ashvin Vishwanath, and Dan M Stamper-Kurn. Ultracold atoms in a tunable optical kagome lattice. *Physical review letters*, 108(4):045305, 2012.
- [8] Maximilian L Kiesel and Ronny Thomale. Sublattice interference in the kagome Hubbard model. *Physical Review B*, 86(12):121105, 2012.
- [9] Xianxin Wu, Tilman Schwemmer, Tobias Müller, Armando Consiglio, Giorgio Sangiovanni, Domenico Di Sante, Yasir Iqbal, Werner Hanke, Andreas P Schnyder, M Michael Denner, et al. Nature of unconventional pairing in the kagome superconductors AV_3Sb_5 ($A=K, Rb, Cs$). *Physical review letters*, 127(17):177001, 2021.
- [10] Yu-Xiao Jiang, Jia-Xin Yin, M Michael Denner, Nana Shumiya, Brenden R Ortiz, Gang Xu, Zurab Guguchia, Junyi He, Md Shafayat Hossain, Xiaoxiong Liu, et al. Unconventional chiral charge order in kagome superconductor KV_3Sb_5 . *Nature materials*, 20(10):1353–1357, 2021.
- [11] Mingu Kang, Shiang Fang, Jonggyu Yoo, Brenden R Ortiz, Yuzki M Oey, Jonghyeok Choi, Sae Hee Ryu, Jimin Kim, Chris Jozwiak, Aaron Bostwick, et al. Charge order landscape and competition with superconductivity in kagome metals. *Nature Materials*, 22(2):186–193, 2023.

- [12] Zuowei Liang, Xingyuan Hou, Fan Zhang, Wanru Ma, Ping Wu, Zongyuan Zhang, Fanghang Yu, J-J Ying, Kun Jiang, Lei Shan, et al. Three-dimensional charge density wave and surface-dependent vortex-core states in a kagome superconductor CsV_3Sb_5 . *Physical Review X*, 11(3):031026, 2021.
- [13] Yaojia Wang, Shuo-Ying Yang, Pranava K Sivakumar, Brenden R Ortiz, Samuel ML Teicher, Heng Wu, Abhay K Srivastava, Chirag Garg, Defa Liu, Stuart SP Parkin, et al. Anisotropic proximity-induced superconductivity and edge supercurrent in kagome metal, $\text{K}_1\text{-xV}_3\text{Sb}_5$. *Science advances*, 9(28):eadg7269, 2023.
- [14] Hong Li, He Zhao, Brenden R Ortiz, Takamori Park, Mengxing Ye, Leon Balents, Ziqiang Wang, Stephen D Wilson, and Ilija Zeljkovic. Rotation symmetry breaking in the normal state of a kagome superconductor KV_3Sb_5 . *Nature Physics*, 18(3):265–270, 2022.
- [15] Jun Wen, Andreas Rüegg, C-C Joseph Wang, and Gregory A Fiete. Interaction-driven topological insulators on the kagome and the decorated honeycomb lattices. *Physical Review B—Condensed Matter and Materials Physics*, 82(7):075125, 2010.
- [16] Wan-Sheng Wang, Zheng-Zhao Li, Yuan-Yuan Xiang, and Qiang-Hua Wang. Competing electronic orders on kagome lattices at Van Hove filling. *Physical Review B—Condensed Matter and Materials Physics*, 87(11):115135, 2013.
- [17] Maximilian L Kiesel, Christian Platt, and Ronny Thomale. Unconventional

- Fermi surface instabilities in the kagome Hubbard model. *Physical review letters*, 110(12):126405, 2013.
- [18] Yu-Ping Lin and Rahul M Nandkishore. Complex charge density waves at Van Hove singularity on hexagonal lattices: Haldane-model phase diagram and potential realization in the kagome metals AV_3Sb_5 ($A=K, Rb, Cs$). *Physical Review B*, 104(4):045122, 2021.
- [19] Harley D Scammell, Julian Ingham, Tommy Li, and Oleg P Sushkov. Chiral excitonic order from twofold Van Hove singularities in kagome metals. *Nature Communications*, 14(1):605, 2023.
- [20] Pranab Kumar Nag, Rajib Batabyal, Julian Ingham, Noam Morali, Hengxin Tan, Jahyun Koo, Armando Consiglio, Enke Liu, Nurit Avraham, Raquel Queiroz, et al. Pomeranchuk instability induced by an emergent higher-order Van Hove singularity on the distorted kagome surface of $Co_3 Sn_2 S_2$. *arXiv preprint arXiv:2410.01994*, 2024.
- [21] Yu-Xiao Jiang, Sen Shao, Wei Xia, M Michael Denner, Julian Ingham, Md Shafayat Hossain, Qingzheng Qiu, Xiquan Zheng, Hongyu Chen, Zi-Jia Cheng, et al. Van Hove annihilation and nematic instability on a kagome lattice. *Nature Materials*, 23(9):1214–1221, 2024.
- [22] Alex Shtyk, Garry Goldstein, and Claudio Chamon. Electrons at the monkey saddle: A multicritical Lifshitz point. *Physical Review B*, 95(3):035137, 2017.

- [23] Taige Wang, Noah F. Q. Yuan, and Liang Fu. Moiré surface states and enhanced superconductivity in topological insulators. *Phys. Rev. X*, 11:021024, Apr 2021.
- [24] Yury Sherkunov and Joseph J Betouras. Electronic phases in twisted bilayer graphene at magic angles as a result of Van Hove singularities and interactions. *Physical Review B*, 98(20):205151, 2018.
- [25] Noah FQ Yuan, Hiroki Isobe, and Liang Fu. Magic of high-order Van Hove singularity. *Nature communications*, 10(1):5769, 2019.
- [26] Dmitry V Efremov, Alex Shtyk, Andreas W Rost, Claudio Chamon, Andrew P Mackenzie, and Joseph J Betouras. Multicritical Fermi surface topological transitions. *Physical Review Letters*, 123(20):207202, 2019.
- [27] Alexander Kerelsky, Leo J McGilly, Dante M Kennes, Lede Xian, Matthew Yankowitz, Shaowen Chen, K Watanabe, T Taniguchi, James Hone, Cory Dean, et al. Maximized electron interactions at the magic angle in twisted bilayer graphene. *Nature*, 572(7767):95–100, 2019.
- [28] Yu-Ping Lin and Rahul M Nandkishore. Parquet renormalization group analysis of weak-coupling instabilities with multiple high-order Van Hove points inside the Brillouin zone. *Physical Review B*, 102(24):245122, 2020.
- [29] Laura Classen, Andrey V Chubukov, Carsten Honerkamp, and Michael M Scherer. Competing orders at higher-order Van Hove points. *Physical Review B*, 102(12):125141, 2020.

- [30] Yi-Ting Hsu, Fengcheng Wu, and S Das Sarma. Spin-valley locked instabilities in moiré transition metal dichalcogenides with conventional and higher-order Van Hove singularities. *Physical Review B*, 104(19):195134, 2021.
- [31] Zhen Bi and Liang Fu. Excitonic density wave and spin-valley superfluid in bilayer transition metal dichalcogenide. *Nature communications*, 12(1):642, 2021.
- [32] Mingu Kang, Shiang Fang, Jeong-Kyu Kim, Brenden R Ortiz, Sae Hee Ryu, Jimin Kim, Jonggyu Yoo, Giorgio Sangiovanni, Domenico Di Sante, Byeong-Gyu Park, et al. Twofold Van Hove singularity and origin of charge order in topological kagome superconductor CsV_3Sb_5 . *Nature Physics*, 18(3):301–308, 2022.
- [33] Yong Hu, Xianxin Wu, Brenden R Ortiz, Sailong Ju, Xinloong Han, Junzhang Ma, Nicholas C Plumb, Milan Radovic, Ronny Thomale, Stephen D Wilson, et al. Rich nature of Van Hove singularities in kagome superconductor CsV_3Sb_5 . *Nature Communications*, 13(1):2220, 2022.
- [34] Yi-Ming Wu, Zhengzhi Wu, and Hong Yao. Pair-density-wave and chiral superconductivity in twisted bilayer transition metal dichalcogenides. *Physical Review Letters*, 130(12):126001, 2023.
- [35] AA Abrikosov, JC Campuzano, and K Gofron. Experimentally observed extended saddle point singularity in the energy spectrum of $\text{YBa}_2\text{Cu}_3\text{O}_{6.9}$ and $\text{YBa}_2\text{Cu}_4\text{O}_8$ and some of the consequences. *Physica C: Superconductivity*, 214(1-2):73–79, 1993.

- [36] K Gofron, JC Campuzano, AA Abrikosov, M Lindroos, A Bansil, H Ding, D Koelling, and B Dabrowski. Observation of an "extended" Van Hove singularity in $\text{YBa}_2\text{Cu}_4\text{O}_8$ by ultrahigh energy resolution angle-resolved photoemission. *Physical review letters*, 73(24):3302, 1994.
- [37] Pedro Castro, Daniel Shaffer, Yi-Ming Wu, and Luiz H Santos. Emergence of the Chern supermetal and pair-density wave through higher-order Van Hove singularities in the Haldane-Hubbard model. *Physical Review Letters*, 131(2):026601, 2023.
- [38] Ömer M Aksoy, Anirudh Chandrasekaran, Apoorv Tiwari, Titus Neupert, Claudio Chamon, and Christopher Mudry. Single monkey-saddle singularity of a Fermi surface and its instabilities. *Physical Review B*, 107(20):205129, 2023.
- [39] Lakshmi Pullasserri and Luiz H Santos. Chern bands with higher-order Van Hove singularities on topological moiré surface states. *Physical Review B*, 110(11):115125, 2024.
- [40] F. D. M. Haldane. Model for a quantum Hall effect without Landau levels: Condensed-matter realization of the "parity anomaly". *Phys. Rev. Lett.*, 61:2015–2018, Oct 1988.
- [41] Doron L Bergman, Congjun Wu, and Leon Balents. Band touching from real-space topology in frustrated hopping models. *Physical Review B—Condensed Matter and Materials Physics*, 78(12):125104, 2008.

- [42] Yi Xiao, Vincent Pelletier, Paul M Chaikin, and David A Huse. Landau levels in the case of two degenerate coupled bands: Kagomé lattice tight-binding spectrum. *Physical Review B*, 67(10):104505, 2003.
- [43] Congjun Wu, Doron Bergman, Leon Balents, and S Das Sarma. Flat bands and Wigner crystallization in the honeycomb optical lattice. *Physical review letters*, 99(7):070401, 2007.
- [44] Titus Neupert, Luiz Santos, Claudio Chamon, and Christopher Mudry. Fractional quantum Hall states at zero magnetic field. *Phys. Rev. Lett.*, 106:236804, Jun 2011.
- [45] D. N. Sheng, Zheng-Cheng Gu, Kai Sun, and L. Sheng. Fractional quantum Hall effect in the absence of Landau levels. *Nature Communications*, 2:389 EP –, 07 2011.
- [46] Evelyn Tang, Jia-Wei Mei, and Xiao-Gang Wen. High-temperature fractional quantum Hall states. *Phys. Rev. Lett.*, 106:236802, Jun 2011.
- [47] Kai Sun, Zhengcheng Gu, Hosho Katsura, and S. Das Sarma. Nearly flatbands with nontrivial topology. *Phys. Rev. Lett.*, 106:236803, Jun 2011.
- [48] N. Regnault and B. Andrei Bernevig. Fractional Chern insulator. *Phys. Rev. X*, 1:021014, Dec 2011.
- [49] Yi-Ming Wu, Ronny Thomale, and S Raghu. Sublattice interference promotes

- pair density wave order in kagome metals. *Physical Review B*, 108(8):L081117, 2023.
- [50] Tilman Schwemmer, Hendrik Hohmann, Matteo Dürnagel, Janik Potten, Jacob Beyer, Stephan Rachel, Yi-Ming Wu, Srinivas Raghu, Tobias Müller, Werner Hanke, and Ronny Thomale. Pair density wave instability in the kagome Hubbard model, 2023.
- [51] Gregor Jotzu, Michael Messer, Rémi Desbuquois, Martin Lebrat, Thomas Uehlinger, Daniel Greif, and Tilman Esslinger. Experimental realization of the topological Haldane model with ultracold fermions. *Nature*, 515(7526):237–240, 2014.
- [52] Brenden R Ortiz, Samuel ML Teicher, Yong Hu, Julia L Zuo, Paul M Sarte, Emily C Schueller, AM Milinda Abeykoon, Matthew J Krogstad, Stephan Rosenkranz, Raymond Osborn, et al. CsV₃Sb₅: A Z₂ topological kagome metal with a superconducting ground state. *Physical Review Letters*, 125(24):247002, 2020.
- [53] Kun Jiang, Tao Wu, Jia-Xin Yin, Zhenyu Wang, M Zahid Hasan, Stephen D Wilson, Xianhui Chen, and Jiangping Hu. Kagome superconductors AV₃Sb₅ (A= K, Rb, Cs). *National Science Review*, 10(2):nwac199, 2023.
- [54] Hengxin Tan, Yiyang Jiang, Gregory T McCandless, Julia Y Chan, and Binghai Yan. Three-dimensional higher-order saddle-point-induced flatbands in co-based kagome metals. *Physical Review Research*, 6(4):043132, 2024.

- [55] PS Jessen and IH Deutsch. Optical lattices. *Advances in Atomic, Molecular, and Optical Physics*, 37:95–138, 1996.
- [56] Immanuel Bloch. Ultracold quantum gases in optical lattices. *Nature physics*, 1(1):23–30, 2005.
- [57] Immanuel Bloch and Markus Greiner. Exploring quantum matter with ultracold atoms in optical lattices. *Advances in atomic, molecular, and optical physics*, 52:1–47, 2005.
- [58] Nathan Goldman, Jan C Budich, and Peter Zoller. Topological quantum matter with ultracold gases in optical lattices. *Nature Physics*, 12(7):639–645, 2016.
- [59] Tsz-Him Leung, Malte N Schwarz, Shao-Wen Chang, Charles D Brown, Govind Unnikrishnan, and Dan Stamper-Kurn. Interaction-enhanced group velocity of bosons in the flat band of an optical kagome lattice. *Physical Review Letters*, 125(13):133001, 2020.
- [60] Thomas H Barter, Tsz-Him Leung, Masayuki Okano, Maxwell Block, Norman Y Yao, and Dan M Stamper-Kurn. Spatial coherence of a strongly interacting bose gas in the trimerized kagome lattice. *Physical Review A*, 101(1):011601, 2020.
- [61] SA Parameswaran, Itamar Kimchi, Ari M Turner, DM Stamper-Kurn, and Ashvin Vishwanath. Wannier permanent wave functions for featureless

- bosonic mott insulators;? format?¿ on the 1/3-filled kagome lattice. *Physical review letters*, 110(12):125301, 2013.
- [62] Philipp Hauke, Olivier Tieleman, Alessio Celi, Christoph Ölschläger, Juliette Simonet, Julian Struck, Malte Weinberg, Patrick Windpassinger, Klaus Sengstock, Maciej Lewenstein, et al. Non-abelian gauge fields and topological insulators in shaken optical lattices. *Physical review letters*, 109(14):145301, 2012.
- [63] Karina Jimenez-Garcia, Lindsay J LeBlanc, Ross A Williams, Matthew C Beeler, Abigail R Perry, and Ian B Spielman. Peierls substitution in an engineered lattice potential. *Physical review letters*, 108(22):225303, 2012.
- [64] Léon Van Hove. The occurrence of singularities in the elastic frequency distribution of a crystal. *Phys. Rev.*, 89:1189–1193, Mar 1953.
- [65] Takahiro Fukui, Yasuhiro Hatsugai, and Hiroshi Suzuki. Chern numbers in discretized Brillouin zone: efficient method of computing (spin) Hall conductances. *Journal of the Physical Society of Japan*, 74(6):1674–1677, 2005.
- [66] Anirudh Chandrasekaran, Alex Shtyk, Joseph J. Betouras, and Claudio Chamon. Catastrophe theory classification of Fermi surface topological transitions in two dimensions. *Phys. Rev. Res.*, 2:013355, Mar 2020.
- [67] Noah F. Q. Yuan and Liang Fu. Classification of critical points in energy bands based on topology, scaling, and symmetry. *Phys. Rev. B*, 101:125120, Mar 2020.
- [68] Xiaokun Teng, Ji Seop Oh, Hengxin Tan, Lebing Chen, Jianwei Huang, Bin Gao,

Jia-Xin Yin, Jiun-Haw Chu, Makoto Hashimoto, Donghui Lu, et al. Magnetism and charge density wave order in kagome FeGe. *Nature physics*, 19(6):814–822, 2023.

[69] Xiaokun Teng, Lebing Chen, Feng Ye, Elliott Rosenberg, Zhaoyu Liu, Jia-Xin Yin, Yu-Xiao Jiang, Ji Seop Oh, M Zahid Hasan, Kelly J Neubauer, et al. Discovery of charge density wave in a kagome lattice antiferromagnet. *Nature*, 609(7927):490–495, 2022.

[70] Jia-Xin Yin, Yu-Xiao Jiang, Xiaokun Teng, Md Shafayat Hossain, Sougata Mardanya, Tay-Rong Chang, Zijin Ye, Gang Xu, M Michael Denner, Titus Neupert, et al. Discovery of charge order and corresponding edge state in kagome magnet fege. *Physical review letters*, 129(16):166401, 2022.